Interlayer excitons in MoSe2/2D perovskite hybrid heterostructures – the interplay between charge and energy transfer

Karpińska, M.; Jasiński, J.; Kempt, R.; Ziegler, J. D.; Sansom, H.; Snaith, H. J.; Taniguchi, T.; Watanabe, K.; Surrente, A.; Dyksik, M.; Maude, D. K.; Kłopotowski, Ł.; Chernikov, A.; Kuc, A. B.; Baranowski, M.; Plochocka, P.;

Originally published:

April 2022

Nanoscale 14(2022), 8085-8094

DOI: https://doi.org/10.1039/D2NR00877G

Charge Transfer Induced Inter-layer Exciton in $MoSe_2$/2D perovskite Hybrid Heterostructures

M. Karpińska,[†,‡,‡‡] J. Jasiński,[¶,‡‡] R. Kempt,[§] J. D. Ziegler,[‖] H. Sansom,[⊥] T. Taniguchi ,[#] K. Watanabe ,[@] H. J. Snaith,[⊥] A. Surrente,[¶] M. Dyksik,[†,△] D. K. Maude,[†] Ł. Kłopotowski,[‡] A. Chernikov,[‖,∇] A. Kuc,[*,††] M. Baranowski,[*,¶] and P. Plochocka[*,†,¶]

†*Laboratoire National des Champs Magnétiques Intenses, UPR 3228, CNRS-UGA-UPS-INSA, Grenoble and Toulouse, France*
‡*Institute of Physics, Polish Academy of Sciences, 02-668 Warsaw, Poland*
¶*Department of Experimental Physics, Faculty of Fundamental Problems of Technology, Wroclaw University of Science and Technology, 50-370 Wroclaw, Poland*
§*Technische Universität Dresden, Bergstr. 66c, 01062 Dresden, Germany*
‖*Department of Physics, University of Regensburg, Regensburg D-93053, Germany*
⊥*University of Oxford, Clarendon Laboratory, Parks Road, Oxford, OX1 3PU, United Kingdom*
#*International Center for Materials Nanoarchitectonics, National Institute for Materials Science, Tsukuba, Ibaraki 305-004, Japan*
@*Research Center for Functional Materials, National Institute for Materials Science, Tsukuba, Ibaraki 305-004, Japan*
△*Department of Experimental Physics, Faculty of Fundamental Problems of Technology, Wroclaw University of Science and Technology, Wroclaw, Poland*
∇*Dresden Integrated Center for Applied Physics and Photonic Materials (IAPP) and Würzburg-Dresden Cluster of Excellence ct.qmat, Technische Universität Dresden, 01062 Dresden, Germany*
††*Helmholtz-Zentrum Dresden-Rossendorf, Permoserstraße 15, 04318 Leipzig, Germany*
‡‡*Contributed equally to this work*

E-mail: a.kuc@hzdr.de; michal.baranowski@pwr.edu.pl; paulina.plochocka@lncmi.cnrs.fr

Abstract

Van der Waals crystals have opened a new and exciting chapter in heterostructure research, removing lattice matching constraints characteristic of epitaxial semiconductors. They provide unprecedented flexibility for heterostructure design. Combining two-dimensional (2D) perovskites with other 2D materials, in particular transition metal dichalcogenides (TMDs) has recently emerged as an intriguing way to design hybrid opto-electronic devices. However, the excitation transfer mechanism between the layers (charge or energy transfer) remains to be elucidated. Here, we investigate $PEA_2PbI_4/MoSe_2$ and $(BA)_2PbI_4/MoSe_2$ heterostructures by combining optical spectroscopy and density functional theory (DFT) calculations. We show that the band alignment facilitates charge transfer. Namely, holes are transferred from the TMD to the 2D perovskite, while the electron transfer is blocked, resulting in the formation of inter-layer excitons. Moreover, we show that the energy transfer mechanism can be turned on by an appropri-

ate alignment of the excitonic states, providing a rule of thumb for the deterministic control of the excitation transfer mechanism in TMD/2D-perovskite heterostructures.

Introduction

Over the past few decades, semiconductor heterostructures have opened a new chapter in material engineering,[1–4] becoming the heart of every-day opto-electronic devices,[5] while providing a rich playground for fundamental solid state physics research.[6,7] The recent rediscovery of layered materials has launched the new era of van der Waals heterostructures, propulsed by their ease of fabrication,[4,8] and almost infinite choice of constituent layered materials, including semiconductors, metals, superconductors, isolators and topological systems.[9–14] In contrast to epitaxial semiconductors, the absence of lattice matching constraints, permits the stacking of an almost unlimited combination of mono and few layers 2D crystals to form heterostructures with new exotic properties.[15–19] Moreover, with simple fabrication technology,[20–22] it is possible to obtain atomically sharp interfaces, and the close proximity of the stacked layers. The band alignment of the layers, together with their spacing, can easily be controlled by the appropriate selection of materials[23–26] This, together with strong excitonic effects,[27–30] make van der Waals heterostructures a very attractive system to investigate charge transfer[31,32] and energy transfer[14,25,26,33] with a view to applications.[34–36]

Among semiconducting layered materials, two families have received particular attentions over the past few years. Namely, transition metal dichalcogenides (TMDs)[27,37] and 2D hybrid perovskites.[38,39] Their fascinating properties make these systems promising candidates for a new generations of opto-electronic and energy harvesting devices.[39–41] Combining these two families of van der Waals crystal, it is possible to produce a new type of hybrid heterostructure. The functional (carrier confining) layers of the hybrid structure are separated by an organic spacer which is an intrinsic part of the 2D perovskites. Despite the rapidly growing interest in this type of heterostructures,[42–46] the excitation transfer mechanism remains to be elucidated. Even in the presence of the wide band gap organic spacer, both types of excitation transfer (*i.e.*, charge or energy transfer) are observed.[42,47] However, the research published to date does not provide general conclusions concerning which mechanism dominates, and whether this can be controlled. This information is of paramount importance if we are to develop deterministic device assembly strategies.

Here, we address this issue for PEPI/$MoSe_2$ and BAPI/$MoSe_2$ heterostructures, where PEPI is $(PEA)_2PbI_4$, PEA is phenylethylammonium, BAPI is $(BA)_2PbI_4$ and BA is buthylammonium (both 2D perovskites are $n = 1$ i.e. the inorganic slab thickens corresponds to single PbI_6 octahedral unit). This investigation, together with our previous work,[48] shows that an appropriate choice of the TMD and the 2D perovskite organic spacer indeed allows to control the excitation transfer mechanism between the layers. The character of excitation transfer depends on the energy matching of the excitonic states between the layers. These conclusions are supported by our experimental and theoretical work, providing for the first time a rule of thumb for the deterministic control of the excitation transfer mechanism in these hybrid heterostructures. Our investigation indicates that, in general, it is the valence band alignment which provide the required conditions for the charge transfer of a hole from the TMD to the perovskite, leading to the formation of an inter-layer excitonic state. At the same time, energy transfer (if present), should transfers excitation from the 2D perovskite to the TMD.

Results

We have used optical spectroscopy to investigate PEPI/$MoSe_2$ and BAPI/$MoSe_2$ heterostructures imaged in Fig. 1 (a-b). Each heterostructure consists of a 2D Ruddlesden-Popper perovskite multi-layer placed on top of monolayer $MoSe_2$. To obtain the best

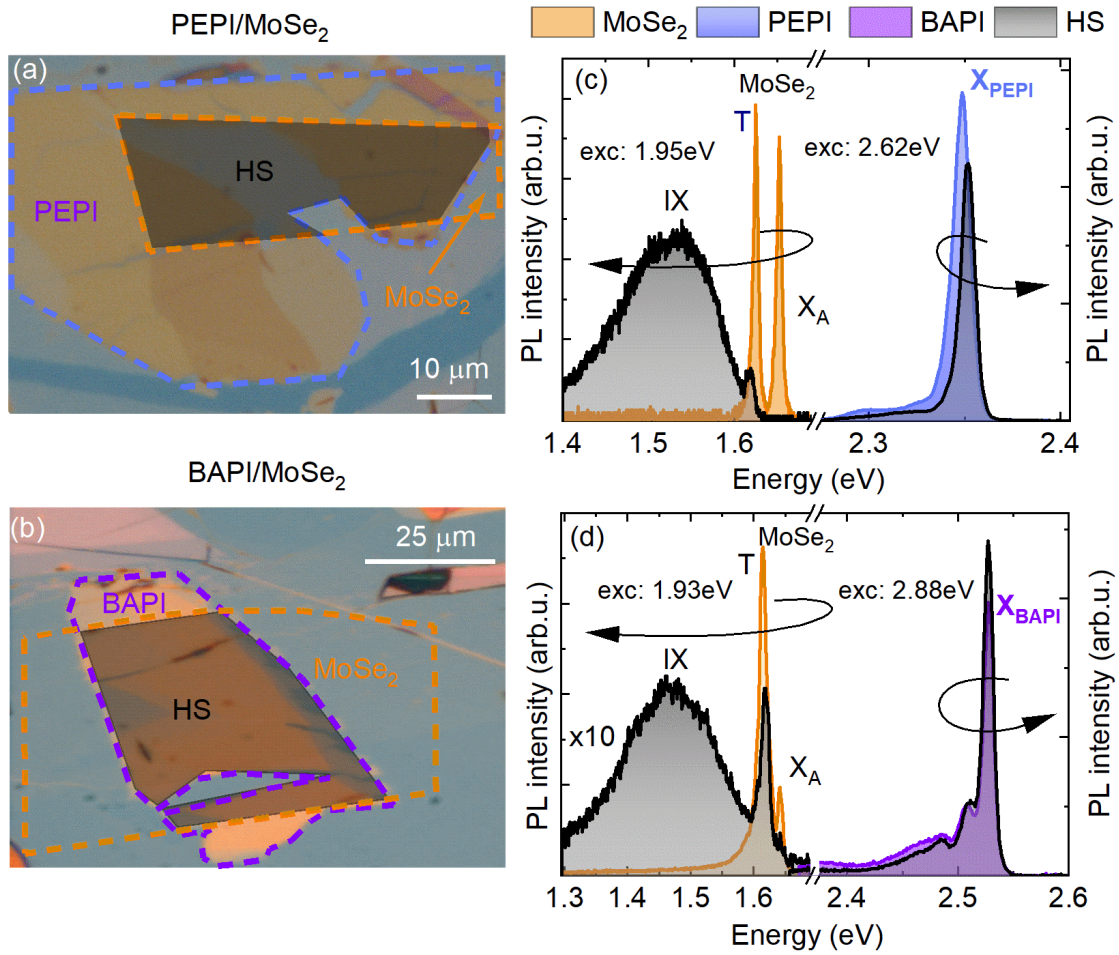

Figure 1: Optical microscope image of (a) PEPI/$MoSe_2$ and (b) BAPI/$MoSe_2$ structures. Blue (violet) dashed lines outline the edges of bare PEPI(BAPI), whereas orange dashed lines outline monolayer $MoSe_2$ flakes. The black shaded area indicates the heterostructure region. PL spectra measured on (c) PEPI/$MoSe_2$ and (d) BAPI/$MoSe_2$ heterostructures. In the heterostructure region an additional low energy (IX) peak is observed.

optical quality, provide environmental protection and stability under light illumination, the heterostructures are encapsulated in hexagonal boron nitride.[49,50] The resulting stacks are placed on a Si/SiO_2 substrate (for details see Methods section).

On the microscope images in Fig.1(a-b), regions of PEPI/BAPI are outlined by dashed blue/violet lines and the $MoSe_2$ monolayer regions are outlined by dashed orange lines. The heterostructure regions are indicated by a darker color where the TMD monolayer and the perovskite overlap. Each region has dimensions of a few microns to tens of microns, which is significantly larger than the spatial resolution of our micro-PL system. Therefore, an optical characterization can easily be performed for either the isolated layers or the heterostructure region.

The observed photoluminescence (PL) spectra of both samples, performed at 5 K are presented in Fig.1 (c-d). To separate the PL response for the different layers, we use lasers with different photon energies. To investigate the PL response from the TMD below 1.7 eV we use 633 nm laser light (1.95 eV) or 640 nm laser light (1.93 eV). This is below the absorption edge of the perovskites, thus avoiding emission from 2D perovskites defects or self-trapped excitons[51] . To excite the PEPI and BAPI layers we use above band gap laser light, above 2.2 eV (473 nm or 430 nm).

The PL emission from the isolated $MoSe_2$ monolayer and 2D perovskite regions are typical for these materials. Two PL peaks, at 1.65 eV and 1.62 eV (orange shading) related to monolayer $MoSe_2$ free exciton (X_A) and negatively charged exciton/trion (T) recombination are

observed.[52] Similarly, for the isolated 2D perovskite regions, strong excitonic PL emission is observed at ∼2.35 eV for PEPI and ∼2.53 eV for BAPI, with characteristic low energy side bands.[30,53,54]

In the heterostructure regions a striking change in the PL spectra is observed for the TMD emission. A strongly broadened peak appears at lower energy (grey shading), which we assign to emission from the inter-layer exciton (IX) with the hole confined in PEPI or BAPI layer and electron in $MoSe_2$ (as we corroborate in the further parts of article). The maximum of this new PL emission is located at ∼1.52 eV for PEPI/$MoSe_2$ and at 1.47 eV for BAPI/$MoSe_2$. Importantly, this new PL feature is observed only in heterostructure regions where the TMD and 2D perovskite layers are in contact. It is completely absent outside of the heterostructure region, as shown in spatially resolved PL maps in Fig.S1 (a-d). Our assignment of the IX transition is confirmed by photoluminescence excitation spectroscopy (see further part of the article) and the orders of magnitude longer PL decay time (see Fig. S2) than normally observed for TMDs[55,56] or 2D perovskite layers[57,58] at low temperature.

The appearance of the IX emission is accompanied by a strong decrease of the $MoSe_2$ excitonic emission (Fig.1(c-d)). For the PEPI/$MoSe_2$ heterostructure, the neutral exciton emission is completely quenched and the trion emission is around ten times lower. For BAPI/$MoSe_2$, weak neutral exciton emission remains (seen as a shoulder) and trion emission is reduced by around 50% .

In both heterostructures, the intensity ratio between negative trion and X_A evidently rises indicating increasing n-type doping (in naturally n-type $MoSe_2$). The increasing doping of $MoSe_2$ is additionally supported by reflectivity spectra, where the trion resonance appears only when TMD layer is in contact with the 2D perovskite (see Fig. S3). These results are indicative of an efficient charge transfer mechanism, where following the excitation, electrons remain in the $MoSe_2$ monolayer, while holes are transferred to perovskite layer, effectively increasing n-type doping of $MoSe_2$ and providing the required conditions for inter-layer exciton formation.

In contrast, changes in the PL corresponding to the perovskite emission are not so pronounced in the heterostructure region. Modifications of the PL intensity are rather moderate with a decrease in PEPI/$MoSe_2$ and increase in BAPI/$MoSe_2$. Since the 2D perovskite multi-layers are much thicker, we expect charge transfer and energy transfer to have a relatively weak impact on the overall emission from the perovskite states due to the significant volume difference between the TMD and the perovskite layers.

Fig. 2 presents the results of DFT band structure calculations for both heterostructures. It is important to note that for the calculations the heterostructure was treated as an ensemble to correctly determine the band alignments[48] (see methods section and SI for more details regarding DFT computations). The TMD and 2D perovskite layers in both cases are incommensurate, thus, larger heterostructures with a twist angle were necessary in order to minimize the strain on the lattices below 0.2%. To reveal the contribution of particular orbitals to the valence and conduction bands we performed Mulliken analysis presented on the right hand side of panels (a) and (b). This shows that the top of the valence band in PEPI- and BAPI- heterostructure is mainly composed of orbitals from the PbI_4 slab, while the conduction bands edges are dominated by the TMD states, as clearly seen in the projected density of states (pDOS) plots. States related to the organic spacers are a few eV above the edges of lowest conduction bands (in both structures) forming barrier for electrons. Similarly in the valence band, the largest contribution of the organic spacer orbitals to the valence band DOS is observed at -6.5 eV and -7.8 eV, for PEPI/$MoSe_2$ and BAPI/$MoSe_2$ respectively, significantly below the top of the $MoSe_2$ and PbI_4 valence bands.

Closer inspection (expanded view of the top of the valence band), reveals a non-vanishing contribution of the organic spacers to the DOS between the valence band edges of PbI_4 and $MoSe_2$. Consequently, a cascade-like band alignment is formed in the valence bands of

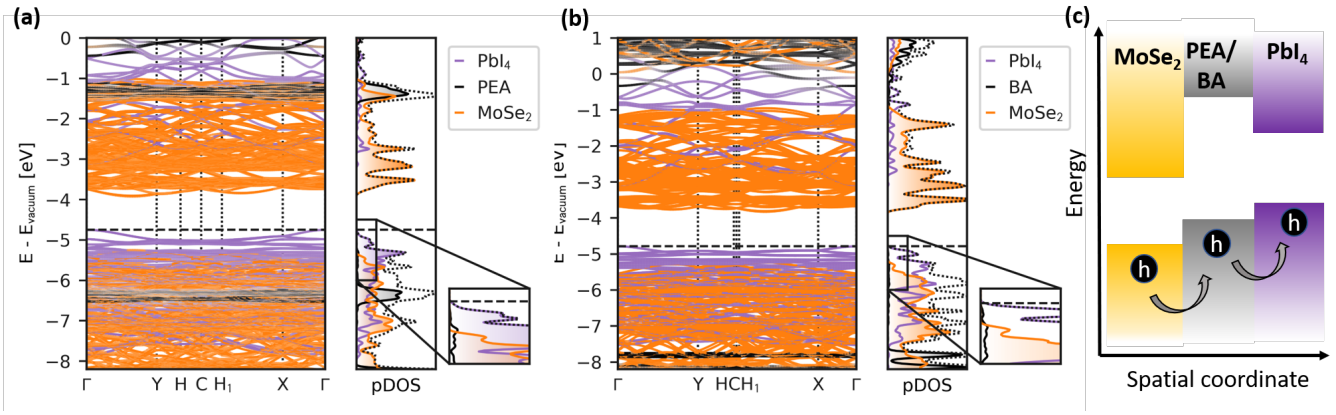

Figure 2: (a) and (b) Mulliken-projected band structure of the PEPI/$MoSe_2$ and BAPI/$MoSe_2$ heterostructure showing the majority contributions of each layer and density of states (pDOS) projected to particular building blocks ($MoSe_2$, PEA or BA, PbI_4). Zoom-in of pDOS shows contribution of organic spacer states between $MoSe_2$ and PbI_4 valence band edges. Both heterostructures indicate type-II band alignment. The valence band maximum (VBM) is localized in the PbI_4 layer at Γ point, while the conduction band minimum (CBM) is localized in the $MoSe_2$ layer at a low-symmetry k point between Γ and Y. (c) Schematic illustration of the band alignment in both heterostructures as calculated by DFT.

both heterostructures, facilitating hole transfer from $MoSe_2$ to the 2D perovskite, (as shown in panel (c) of Fig. 2), providing conditions for inter-layer exciton formation. Therefore, our DFT calculations support the hypothesis that the low energy PL originates from inter-layer exciton (IX) emission with the electron localized in the $MoSe_2$ layer and the hole localized in the 2D perovskite layer. Qualitatively, the same band alignment is observed for WS_2/PEPI,[48] where an effective hole transfer is observed, however, there is no consensus concerning the existence of inter-layer emission in WS_2/PEPI heterostructures.[42,48]

It is worth to note, that the energy of the valence band edge of PEPI and BAPI are at almost the same energy (according to our DFT calculation). Therefore, the gaps between conduction band edge of $MoSe_2$ and valence band edge of PbI_4 are almost the same in both heterostructures. This explains the small change in the energy of the IX emission, when PEPI is replaced by the higher band gap BAPI.Noteworthy, our single-particle DFT results account already for the main experimental observations, what implies that Coulomb corrections (typically obtained from GW or Bethe-Salpeter equation) should not contribute too much or would even cancel each other out.

Importantly, interlayer excitons appear prominently in PLE spectra as shown in Fig.3 (a-b). In both panels the integrated PL intensities of T and IX are normalized to their intensity under the excitation wavelength corresponding to X_B resonance of $MoSe_2$. For both heterostructures we observe an increase of the IX intensity when exciting in resonance with $X_{PEPI/BAPI}$ (2.37/2.55 eV) or X_B in $MoSe_2$. The enhancement of the IX PL emission observed for the resonant excitation with exciton states in either layer, strongly support the inter-layer nature of the IX emission. For example, even though the exciton resonance of PEPI does not correspond to any excitonic transition in $MoSe_2$, an enhancement of the IX PL occurs, indicating that it is related to carriers (more specifically holes) created in the 2D perovskite layer. On the other hand, under resonant excitation with X_B, the particular band alignment favours hole transfer to PbI_4, even if they are created in the $MoSe_2$ layer. Subsequently, Coulomb attraction between electrons in the $MoSe_2$ layer and holes in the 2D perovskite leads to the formation of inter-layer excitons.

The effective hole transfer from $MoSe_2$ to PbI_4 layer is further confirmed by the time resolved PL studies presented in Fig. 3 (c-d). Even when the sample is excited with photon energy of 1.86 eV (significantly below 2D perovskites exciton states), the PL signal related to trion emission decays much faster in the heterostructure region (gray curves) than in bare $MoSe_2$ regions (orange curves). Therefore, the effective transfer of holes to the 2D perovskite

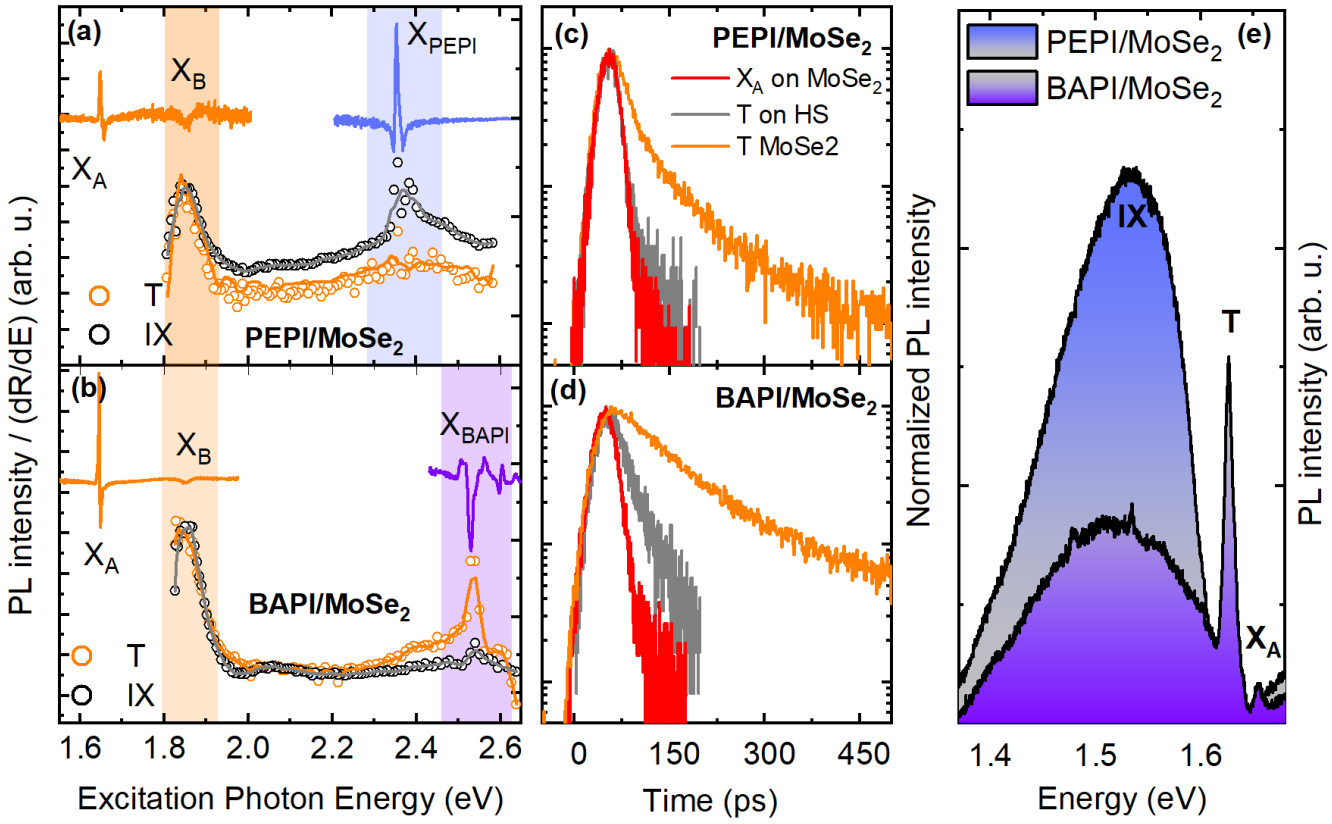

Figure 3: PL intensity versus excitation photon energy for (a) - PEPI/$MoSe_2$ and (b) - BAPI/$MoSe_2$ heterostructure. Integration was performed separately for T (orange) and IX (gray circles). The 1st derivative of reflectivity is also shown (orange solid lines for $MoSe_2$, blue - PEPI and violet - BAPI), excitonic resonances of $MoSe_2$ (1.85 eV - X_B) and 2D perovskites (2.35 eV - PEPI and 2.55 eV - BAPI) are clearly visible. PL decay curves for PEPI/$MoSe_2$ - (c) and BAPI/$MoSe_2$ - (d). Orange and red curves correspond to signal from and T and X_A on bare $MoSe_2$, respectively, and grey curve - signal from T in the heterostructure region. (e) comparison of interlayer exciton PL intensity form PEPI/$MoSe_2$ and BAPI/$MoSe_2$

layers increase the PL decay rate (which is sum of all process rates which decreases the trion population) corroborating our other experimental and theoretical results.

So far we have focused on the similarities between both heterostructures. However, some quantitative difference are seen which provide evidence for an energy transfer between the layers in BAPI/$MoSe_2$. The first difference can be seen in the PLE dependence for the trion transition. While for PEPI/$MoSe_2$ there is almost no change of the trion intensity when exciting in X_{PEPI} (orange circles in Fig. 3 (a)), a clear enhancement of the trion intensity is seen for BAPI/$MoSe_2$ (orange circles in Fig. 3 (b)). Since the calculated band structure exclude electron transfer to the $MoSe_2$ layers (or at least it has to be strongly suppressed), this enhancement has to be related to energy transfer from BAPI to $MoSe_2$. The second and third difference is presented in Fig. 3 (c,d,e). The trion emission in BAPI/$MoSe_2$ is longer than for the PEPI/$MoSe_2$ and IX emission is generally more intense for the PEPI/$MoSe_2$ compared to BAPI/$MoSe_2$ (under same excitation conditions) which may indicate a less effective hole transfer and/or an additional transfer process in the opposite direction, *i.e.* energy transfer from BAPI to $MoSe_2$. Fig. 4 shows that the spectral overlap of different transitions in individual layers provides arguments that energy transfer indeed plays a role. Generally the X_A and X_B transitions in TMDs are significantly below the excitonic states of PEPI and BAPI. Only in the case of WS_2 the X_B transition overlaps with PEPI exited exciton states (2s, 3s, ...) leading to previously reported Förster-like resonant (non-radiative) energy transfer.[42,48] According to the diagram, such a resonance can occur also for WS_2/BAPI.

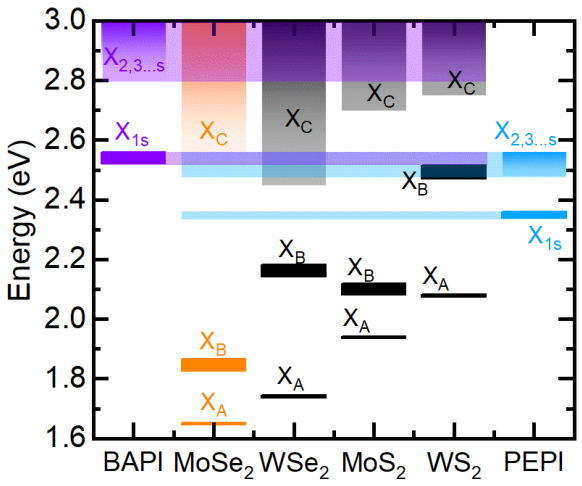

Figure 4: Diagram of excitonic transition energies at cryogenic temperatures in TMDs monolayers and $(BA)_2PbI_4$(BAPI) and $(PEA)_2PbI_4$ (PEPI) 2D perovskites taken after.[59,60,60–63]

For the investigated heterostructures, the 2D perovskite exciton states overlap only with the onset of a broad TMD absorption feature referred to as the C exciton (X_C).[64–67] For PEPI, the overlap occurs only for the excited exciton states and no energy transfer is observed. Crucially for BAPI, the overlap occurs for the 1s states, favoring energy transfer, which is observed as enhanced trion emission Fig.3 (b). This may indicate that the coupling of C exction to PEPI exciton excited state is weak and Förster-like resonant energy transfer is suppressed in this case. In contrast the much higher oscillator strength of 1s transition in BAPI can enhance Förster coupling between the layers. Alternatively the experimental observation can also point that the energy transfer is mediated by photon reabsorption by the C exciton band. The 1s state of BAPI can effectively provide photons (to be absorbed by TMD layer) since it is the ground emissive state of the perovskite layer. In contrast, the exciton excited states in PEPI are poorly emissive due to the fast relaxation of excitons to the ground 1s state.

Conclusions

We have reported a comprehensive investigation of charge and energy transfer in PEPI/$MoSe_2$ and BAPI/$MoSe_2$ hybrid heterostructures. We show that the excitation transfer in both heterostructures is dominated by charger transfer. Our DFT calculation shows that this is related to a cascade band alignment in the valence band of the heterostructure which facilitates hole transfer from $MoSe_2$ to the PbI_4 layer of the perovskite. The effective type II band alignment between $MoSe_2$ and the 2D perovskite gives rise to the formation of inter-layer excitons (IX), with PL emission below the intra-layer excitonic transitions. The inter-layer nature of the IX transition is supported by the long PL decay time and PLE studies. Moreover, for the case of BAPI/$MoSe_2$, energy transfer is observed from the 2D perovskite to $MoSe_2$ monolayer. An analysis of the energies of excitonic transitions in the different layers which might indicate that energy transfer is related to reabsorption of photons in the $MoSe_2$ monolayer, which were emitted by the BAPI 1s ground state.

Methods

Synthesis and sample preparation

To obtain the hybrid samples we used the stamping technique established for inorganic 2D materials outlined in Ref.[68] Thin hBN flakes were first mechanically exfoliated on polydimethylsiloxane (PDMS) from bulk crystals (provided by T. Taniguchi and K. Watanabe, NIMS) and subsequently stamped on a 90°C preheated SiO_2/Si substrate at ambient conditions. After annealing the hBN flakes at 180°C for 1-2 hours, similarly exfoliated monolayer $MoSe_2$ (bulk crystals from hqgraphene) are stamped on top of the hBN at a substrate temperature of 70°C and again annealed at 150°C. Single crystals of PEPI and BAPI were exfoliated and stamped using PDMS in the same way, but without the use of additional heating. The perovskite flakes were immediately fully encapsulated to inhibit degradation.

DFT calculations

Model structures of $MoSe_2$@$(PEA)_2PbI_4$ and $MoSe_2$@$(BA)_2PbI_4$ were created using a coin-

cidence lattice algorithm implemented in hetbuilder[69] with less than 0.2 % strain on the individual layers. The $MoSe_2$@$(PEA)_2PbI_4$ heterostructure consists of 354 atoms and can be characterized by supercell vectors $m_1 = (4, 1)$, $m_2 = (-4, 5)$, $n_1 = (-1, -1)$ and $n_2 = (3, 0)$ with a rotation angle of $\theta = 146.5°$ and a vacuum spacing of 100 Å. The $MoSe_2$@$(BA)_2PbI_4$ heterostructure in the low-temperature phase consists of 207 atoms and can be characterized by supercell vectors $m_1 = (-1, -4)$, $m_2 = (4, 7)$, $n_1 = (0, -1)$ and $n_2 = (1, 2)$ with a rotation angle of $\theta = 20.65°$ and a vacuum spacing of 100 Å, see Ref.[69] for details (other representation choices are possible). These model structures were relaxed using FHI-aims[70] employing the PBE functional[71] on tight tier 1 numeric atom-centered orbitals, including the non-self-consistent Tktchenko-Scheffler correction for dispersion interactions,[72] and scalar relativistic corrections (ZORA) on a $2 \times 2 \times 1$ Γ-centered k-grid. The γ-angle was kept fixed, while forces and stresses were minimized until below 0.01 eV Å^{-1}. The SCF parameters were adjusted automatically after three steps. The electronic band structure, the Mulliken-projections, and the density of states were calculated including spin-orbit coupling (SOC) and considering the dipole correction on a $4 \times 4 \times 1$ Γ-centered k-grid.

Optical measurements

The samples were mounted with the silver paste on the cold finger of a liquid helium-cooled optical cryostat. All the experiments were performed using a home-built setup at the temperature 5 K. The excitation source was halogen or xenon lamp (reflectivity), and continuous wave 633 nm laser diode, 640 nm solid state laser, 473 nm solid state laser, 400 nm pulsed laser diode, supercontinuum laser, second harmonic of a Ti:Sapphire laser or doubled frequency of optical parametric oscillator (PL). The light beam was focused on the sample with a spot of $\simeq 1\mu$m diameter using a microscope objective with numerical aperture of 0.55 and magnification 50×. The same objective then collected the signal from the sample and directed it to a 0.3 m or 0.5 m long spectrometer. A liquid nitrogen-cooled CCD camera was used as the signal detector. For PL measurements, the laser beam was filtered out by a long pass edge filter before entering the monochromator. Spatial PL mapping was performed with the scanning step 1μm along the x and y axes with the use of an automated xy translation stage on which the cryostat was mounted. PLE experiments were conducted using the same setup as the PL measurements. For time-resolved measurements the sample signal was detected by a single photon avalanche photo-diode with 1 ns setup time resolution (long time range) or streak camera with time resolution of 10 ps (short time range).

Acknowledgments

We would like to thank Omer Yaffe and Matan Menaham for providing the PEPI bulk crystals. AK and RK gratefully acknowledge the Gauss Centre for Supercomputing e.V. (www.gauss-centre.eu) for funding this project by providing computing time through the John von Neumann Institute for Computing (NIC) on the GCS Supercomputer JUWELS at Jülich Supercomputing Centre (JSC). Furthermore, AK and RK gratefully acknowledge the GWK support for funding this project by providing computing time through the Center for Information Services and HPC (ZIH) at TU Dresden. AK acknowledges the financial support from Deutsche Forschungsgemeinschaft (DFG, German Research Foundation) within SFB1415 project number 417590517 and the association with the SPP2244 (2DMP). PP and JJ appreciates support from National Science Centre Poland within the OPUS (grant no. 2019/33/B/ST3/01915) and Preludium Bis 1 (2019/35/O/ST3/02162) programs respectively. MD appreciates support from the Polish National Agency for Academic Exchange within the Bekker programme (grant no. PPN/BEK/2019/1/00312/U/00001). This study has been partially supported through the EUR grant NanoX n° ANR-17-EURE-0009 in the framework of the "Programme des In-

vestissements d'Avenir". The Polish participation in European Magnetic Field Laboratory (EMFL) is supported by the DIR/WK/2018/07 grant from Ministry of Science and Higher Education, Poland. KW and TT acknowledge support from the Elemental Strategy Initiative conducted by the MEXT, Japan (Grant Number JPMXP0112101001) and JSPS KAKENHI (Grant Numbers JP19H05790 and JP20H00354). A.C. gratefully acknowledges Deutsche Forschungsgemeinschaft (DFG) for funding through SPP 2196 (CH1672/3-1) and Würzburg-Dresden Cluster of Excellence on Complexity and Topology in Quantum Matter ct.qmat (EXC 2147).

References

(1) CAPASSO, F. Band-Gap Engineering: From Physics and Materials to New Semiconductor Devices. *Science* **1987**, *235*, 172–176.

(2) Singh, J. *Electronic and optoelectronic properties of semiconductor structures*; Cambridge University Press, 2007.

(3) Bastard, G. Wave mechanics applied to semiconductor heterostructures. **1990**,

(4) Geim, A. K.; Grigorieva, I. V. Van der Waals heterostructures. *Nature* **2013**, *499*, 419–425.

(5) Ng, K. K. *Complete guide to semiconductor devices*; Wiley Online Library, 2002.

(6) Peter, Y.; Cardona, M. *Fundamentals of semiconductors: physics and materials properties*; Springer Science & Business Media, 2010.

(7) Miura, N. *Physics of semiconductors in high magnetic fields*; Oxford University Press, 2008; Vol. 15.

(8) Novoselov, K.; Mishchenko, o. A.; Carvalho, o. A.; Neto, A. C. 2D materials and van der Waals heterostructures. *Science* **2016**, *353*.

(9) Mak, K. F.; Lee, C.; Hone, J.; Shan, J.; Heinz, T. F. Atomically thin MoS 2: a new direct-gap semiconductor. *Physical review letters* **2010**, *105*, 136805.

(10) Duan, X.; Wang, C.; Pan, A.; Yu, R.; Duan, X. Two-dimensional transition metal dichalcogenides as atomically thin semiconductors: opportunities and challenges. *Chemical Society Reviews* **2015**, *44*, 8859–8876.

(11) Blatter, G.; Geshkenbein, V. Van der Waals Attraction of Vortices in Anisotropic and Layered Superconductors. *Physical Review Letters* **1996**, *77*, 4958–4961.

(12) Illarionov, Y. Y.; Knobloch, T.; Jech, M.; Lanza, M.; Akinwande, D.; Vexler, M. I.; Mueller, T.; Lemme, M. C.; Fiori, G.; Schwierz, F.; Grasser, T. Insulators for 2D nanoelectronics: the gap to bridge. *Nature Communications* **2020**, *11*.

(13) Klein, D. R.; MacNeill, D.; Lado, J. L.; Soriano, D.; Navarro-Moratalla, E.; Watanabe, K.; Taniguchi, T.; Manni, S.; Canfield, P.; Fernández-Rossier, J.; Jarillo-Herrero, P. Probing magnetism in 2D van der Waals crystalline insulators via electron tunneling. *Science* **2018**, *360*, 1218–1222.

(14) Hu, C. et al. A van der Waals antiferromagnetic topological insulator with weak interlayer magnetic coupling. *Nature Communications* **2020**, *11*.

(15) Rasmita, A.; bo Gao, W. Opto-valleytronics in the 2D van der Waals heterostructure. *Nano Research* **2020**, *14*, 1901–1911.

(16) Wu, F.; Lovorn, T.; Tutuc, E.; MacDonald, A. H. Hubbard model physics in transition metal dichalcogenide moiré bands. *Physical review letters* **2018**, *121*, 026402.

(17) Tang, Y.; Li, L.; Li, T.; Xu, Y.; Liu, S.; Barmak, K.; Watanabe, K.; Taniguchi, T.;

MacDonald, A. H.; Shan, J., et al. Simulation of Hubbard model physics in WSe 2/WS 2 moiré superlattices. *Nature* **2020**, *579*, 353–358.

(18) Tran, K.; Moody, G.; Wu, F.; Lu, X.; Choi, J.; Kim, K.; Rai, A.; Sanchez, D. A.; Quan, J.; Singh, A., et al. Evidence for moiré excitons in van der Waals heterostructures. *Nature* **2019**, *567*, 71–75.

(19) Cao, Y.; Fatemi, V.; Fang, S.; Watanabe, K.; Taniguchi, T.; Kaxiras, E.; Jarillo-Herrero, P. Unconventional superconductivity in magic-angle graphene superlattices. *Nature* **2018**, *556*, 43–50.

(20) Castellanos-Gomez, A.; Buscema, M.; Molenaar, R.; Singh, V.; Janssen, L.; Van Der Zant, H. S.; Steele, G. A. Deterministic transfer of two-dimensional materials by all-dry viscoelastic stamping. *2D Materials* **2014**, *1*, 011002.

(21) Frisenda, R.; Navarro-Moratalla, E.; Gant, P.; De Lara, D. P.; Jarillo-Herrero, P.; Gorbachev, R. V.; Castellanos-Gomez, A. Recent progress in the assembly of nanodevices and van der Waals heterostructures by deterministic placement of 2D materials. *Chemical Society Reviews* **2018**, *47*, 53–68.

(22) Pizzocchero, F.; Gammelgaard, L.; Jessen, B. S.; Caridad, J. M.; Wang, L.; Hone, J.; Bøggild, P.; Booth, T. J. The hot pick-up technique for batch assembly of van der Waals heterostructures. *Nature Communications* **2016**, *7*.

(23) Kang, J.; Tongay, S.; Zhou, J.; Li, J.; Wu, J. Band offsets and heterostructures of two-dimensional semiconductors. *Applied Physics Letters* **2013**, *102*, 012111.

(24) Özcelik, V. O.; Azadani, J. G.; Yang, C.; Koester, S. J.; Low, T. Band alignment of two-dimensional semiconductors for designing heterostructures with momentum space matching. *Physical Review B* **2016**, *94*, 035125.

(25) Liu, X.; Pei, J.; Hu, Z.; Zhao, W.; Liu, S.; Amara, M.-R.; Watanabe, K.; Taniguchi, T.; Zhang, H.; Xiong, Q. Manipulating charge and energy transfer between 2D atomic layers via heterostructure engineering. *Nano Letters* **2020**, *20*, 5359–5366.

(26) Xu, W.; Kozawa, D.; Liu, Y.; Sheng, Y.; Wei, K.; Koman, V. B.; Wang, S.; Wang, X.; Jiang, T.; Strano, M. S., et al. Determining the optimized interlayer separation distance in vertical stacked 2D WS2: hBN: MoS2 heterostructures for exciton energy transfer. *Small* **2018**, *14*, 1703727.

(27) Wang, Q. H.; Kalantar-Zadeh, K.; Kis, A.; Coleman, J. N.; Strano, M. S. Electronics and optoelectronics of two-dimensional transition metal dichalcogenides. *Nature Nanotechnology* **2012**, *7*, 699–712.

(28) Mak, K. F.; Shan, J. Photonics and optoelectronics of 2D semiconductor transition metal dichalcogenides. *Nature Photonics* **2016**, *10*, 216–226.

(29) Wang, G.; Chernikov, A.; Glazov, M. M.; Heinz, T. F.; Marie, X.; Amand, T.; Urbaszek, B. Colloquium: Excitons in atomically thin transition metal dichalcogenides. *Reviews of Modern Physics* **2018**, *90*, 021001.

(30) Blancon, J.-C.; Stier, A. V.; Tsai, H.; Nie, W.; Stoumpos, C. C.; Traore, B.; Pedesseau, L.; Kepenekian, M.; Katsutani, F.; Noe, G., et al. Scaling law for excitons in 2D perovskite quantum wells. *Nature communications* **2018**, *9*, 1–10.

(31) Latini, S.; Winther, K. T.; Olsen, T.; Thygesen, K. S. Interlayer Excitons and Band Alignment in MoS2/hBN/WSe2 van der Waals Heterostructures. *Nano Letters* **2017**, *17*, 938–945.

(32) Rivera, P.; Yu, H.; Seyler, K. L.; Wilson, N. P.; Yao, W.; Xu, X. Interlayer valley excitons in heterobilayers of transition

metal dichalcogenides. *Nature Nanotechnology* **2018**, *13*, 1004–1015.

(33) Kozawa, D.; Carvalho, A.; Verzhbitskiy, I.; Giustiniano, F.; Miyauchi, Y.; Mouri, S.; Castro Neto, A.; Matsuda, K.; Eda, G. Evidence for fast interlayer energy transfer in MoSe2/WS2 heterostructures. *Nano letters* **2016**, *16*, 4087–4093.

(34) Lee, C.-H.; Lee, G.-H.; van der Zande, A. M.; Chen, W.; Li, Y.; Han, M.; Cui, X.; Arefe, G.; Nuckolls, C.; Heinz, T. F.; Guo, J.; Hone, J.; Kim, P. Atomically thin p–n junctions with van der Waals heterointerfaces. *Nature Nanotechnology* **2014**, *9*, 676–681.

(35) Ippolito, S.; Kelly, A. G.; de Oliveira, R. F.; Stoeckel, M.-A.; Iglesias, D.; Roy, A.; Downing, C.; Bian, Z.; Lombardi, L.; Samad, Y. A.; Nicolosi, V.; Ferrari, A. C.; Coleman, J. N.; Samorì, P. Covalently interconnected transition metal dichalcogenide networks via defect engineering for high-performance electronic devices. *Nature Nanotechnology* **2021**, *16*, 592–598.

(36) Withers, F.; Pozo-Zamudio, O. D.; Mishchenko, A.; Rooney, A. P.; Gholinia, A.; Watanabe, K.; Taniguchi, T.; Haigh, S. J.; Geim, A. K.; Tartakovskii, A. I.; Novoselov, K. S. Light-emitting diodes by band-structure engineering in van der Waals heterostructures. *Nature Materials* **2015**, *14*, 301–306.

(37) Manzeli, S.; Ovchinnikov, D.; Pasquier, D.; Yazyev, O. V.; Kis, A. 2D transition metal dichalcogenides. *Nature Reviews Materials* **2017**, *2*.

(38) Grancini, G.; Nazeeruddin, M. K. Dimensional tailoring of hybrid perovskites for photovoltaics. *Nature Reviews Materials* **2018**, *4*, 4–22.

(39) Chen, Y.; Sun, Y.; Peng, J.; Tang, J.; Zheng, K.; Liang, Z. 2D Ruddlesden–Popper perovskites for optoelectronics. *Advanced Materials* **2018**, *30*, 1703487.

(40) Xia, M.; Yuan, J.-H.; Luo, J.; Pan, W.; Wu, H.; Chen, Q.; Xue, K.-H.; Miao, X.; Niu, G.; Tang, J. Two-dimensional perovskites as sensitive strain sensors. *Journal of Materials Chemistry C* **2020**, *8*, 3814–3820.

(41) Tsai, H.; Nie, W.; Blancon, J.-C.; Stoumpos, C. C.; Asadpour, R.; Harutyunyan, B.; Neukirch, A. J.; Verduzco, R.; Crochet, J. J.; Tretiak, S., et al. High-efficiency two-dimensional Ruddlesden–Popper perovskite solar cells. *Nature* **2016**, *536*, 312–316.

(42) Zhang, Q.; Linardy, E.; Wang, X.; Eda, G. Excitonic Energy Transfer in Heterostructures of Quasi-2D Perovskite and Monolayer WS2. *ACS Nano* **2020**, *14*, 11482–11489.

(43) Chen, Y.; Liu, Z.; Li, J.; Cheng, X.; Ma, J.; Wang, H.; Li, D. Robust Interlayer Coupling in Two-Dimensional Perovskite/Monolayer Transition Metal Dichalcogenide Heterostructures. *ACS Nano* **2020**, *14*, 10258–10264.

(44) Chen, Y.; Ma, J.; Liu, Z.; Li, J.; Duan, X.; Li, D. Manipulation of Valley Pseudospin by Selective Spin Injection in Chiral Two-Dimensional Perovskite/Monolayer Transition Metal Dichalcogenide Heterostructures. *ACS Nano* **2020**, *14*, 15154–15160.

(45) Wang, Q.; Zhang, Q.; Luo, X.; Wang, J.; Zhu, R.; Liang, Q.; Zhang, L.; Yong, J. Z.; Yu Wong, C. P.; Eda, G., et al. Optoelectronic Properties of a van der Waals WS2 Monolayer/2D Perovskite Vertical Heterostructure. *ACS Applied Materials & Interfaces* **2020**, *12*, 45235–45242.

(46) Fu, Q.; Wang, X.; Liu, F.; Dong, Y.; Liu, Z.; Zheng, S.; Chaturvedi, A.; Zhou, J.; Hu, P.; Zhu, Z., et al. Ultrathin Ruddlesden–Popper Perovskite Heterojunction for Sensitive Photodetection. *Small* **2019**, *15*, 1902890.

(47) Yang, A.; Blancon, J.-C.; Jiang, W.; Zhang, H.; Wong, J.; Yan, E.; Lin, Y.-R.; Crochet, J.; Kanatzidis, M. G.; Jariwala, D.; Low, T.; Mohite, A. D.; Atwater, H. A. Giant Enhancement of Photoluminescence Emission in WS2-Two-Dimensional Perovskite Heterostructures. *Nano Letters* **2019**, *19*, 4852–4860.

(48) Karpińska, M.; Liang, M.; Kempt, R.; Finzel, K.; Kamminga, M.; Dyksik, M.; Zhang, N.; Knodlseder, C.; Maude, D. K.; Baranowski, M.; Kłopotowski, Ł.; Ye, J.; Kuc, A.; Plochocka, P. Nonradiative Energy Transfer and Selective Charge Transfer in a WS2/(PEA)2PbI4 Heterostructure. *ACS Applied Materials & Interfaces* **2021**, *13*, 33677–33684.

(49) Ziegler, J. D.; Zipfel, J.; Meisinger, B.; Menahem, M.; Zhu, X.; Taniguchi, T.; Watanabe, K.; Yaffe, O.; Egger, D. A.; Chernikov, A. Fast and anomalous exciton diffusion in two-dimensional hybrid perovskites. *Nano Letters* **2020**, *20*, 6674–6681.

(50) Cadiz, F.; Courtade, E.; Robert, C.; Wang, G.; Shen, Y.; Cai, H.; Taniguchi, T.; Watanabe, K.; Carrere, H.; Lagarde, D., et al. Excitonic linewidth approaching the homogeneous limit in MoS 2-based van der Waals heterostructures. *Physical Review X* **2017**, *7*, 021026.

(51) Booker, E. P.; Thomas, T. H.; Quarti, C.; Stanton, M. R.; Dashwood, C. D.; Gillett, A. J.; Richter, J. M.; Pearson, A. J.; Davis, N. J.; Sirringhaus, H., et al. Formation of long-lived color centers for broadband visible light emission in low-dimensional layered perovskites. *Journal of the American Chemical Society* **2017**, *139*, 18632–18639.

(52) Ross, J. S.; Wu, S.; Yu, H.; Ghimire, N. J.; Jones, A. M.; Aivazian, G.; Yan, J.; Mandrus, D. G.; Xiao, D.; Yao, W., et al. Electrical control of neutral and charged excitons in a monolayer semiconductor. *Nature communications* **2013**, *4*, 1–6.

(53) Straus, D. B.; Hurtado Parra, S.; Iotov, N.; Gebhardt, J.; Rappe, A. M.; Subotnik, J. E.; Kikkawa, J. M.; Kagan, C. R. Direct observation of electron–phonon coupling and slow vibrational relaxation in organic–inorganic hybrid perovskites. *Journal of the American Chemical Society* **2016**, *138*, 13798–13801.

(54) Straus, D. B.; Iotov, N.; Gau, M. R.; Zhao, Q.; Carroll, P. J.; Kagan, C. R. Longer cations increase energetic disorder in excitonic 2D hybrid perovskites. *The journal of physical chemistry letters* **2019**, *10*, 1198–1205.

(55) Korn, T.; Heydrich, S.; Hirmer, M.; Schmutzler, J.; Schüller, C. Low-temperature photocarrier dynamics in monolayer MoS2. *Applied Physics Letters* **2011**, *99*, 102109.

(56) Robert, C.; Lagarde, D.; Cadiz, F.; Wang, G.; Lassagne, B.; Amand, T.; Balocchi, A.; Renucci, P.; Tongay, S.; Urbaszek, B., et al. Exciton radiative lifetime in transition metal dichalcogenide monolayers. *Physical review B* **2016**, *93*, 205423.

(57) Fang, H.-h.; Yang, J.; Adjokatse, S.; Tekelenburg, E.; Kamminga, M. E.; Duim, H.; Ye, J.; Blake, G. R.; Even, J.; Loi, M. A. Band-edge exciton fine structure and exciton recombination dynamics in single crystals of layered hybrid perovskites. *Advanced Functional Materials* **2020**, *30*, 1907979.

(58) Folpini, G.; Cortecchia, D.; Petrozza, A.; Kandada, A. R. S. The role of a dark exciton reservoir in the luminescence efficiency of two-dimensional tin iodide perovskites. *Journal of Materials Chemistry C* **2020**, *8*, 10889–10896.

(59) Arora, A.; Nogajewski, K.; Molas, M.; Koperski, M.; Potemski, M. Exciton band

structure in layered MoSe 2: from a monolayer to the bulk limit. *Nanoscale* **2015**, *7*, 20769–20775.

(60) Hanbicki, A.; Currie, M.; Kioseoglou, G.; Friedman, A.; Jonker, B. Measurement of high exciton binding energy in the monolayer transition-metal dichalcogenides WS2 and WSe2. *Solid State Communications* **2015**, *203*, 16–20.

(61) Zhu, B.; Chen, X.; Cui, X. Exciton binding energy of monolayer WS 2. *Scientific reports* **2015**, *5*, 1–5.

(62) Mak, K. F.; He, K.; Shan, J.; Heinz, T. F. Control of valley polarization in monolayer MoS 2 by optical helicity. *Nature nanotechnology* **2012**, *7*, 494–498.

(63) Frisenda, R.; Niu, Y.; Gant, P.; Molina-Mendoza, A. J.; Schmidt, R.; Bratschitsch, R.; Liu, J.; Fu, L.; Dumcenco, D.; Kis, A., et al. Micro-reflectance and transmittance spectroscopy: a versatile and powerful tool to characterize 2D materials. *Journal of Physics D: Applied Physics* **2017**, *50*, 074002.

(64) Hill, H. M.; Rigosi, A. F.; Roquelet, C.; Chernikov, A.; Berkelbach, T. C.; Reichman, D. R.; Hybertsen, M. S.; Brus, L. E.; Heinz, T. F. Observation of Excitonic Rydberg States in Monolayer MoS2 and WS2 by Photoluminescence Excitation Spectroscopy. *Nano Letters* **2015**, *15*, 2992–2997.

(65) Bieniek, M.; Szulakowska, L.; Hawrylak, P. Band nesting and exciton spectrum in monolayer MoS2. *Physical Review B* **2020**, *101*, 125423.

(66) Zhao, W.; Ribeiro, R. M.; Eda, G. Electronic Structure and Optical Signatures of Semiconducting Transition Metal Dichalcogenide Nanosheets. *Accounts of Chemical Research* **2014**, *48*, 91–99.

(67) Kozawa, D.; Kumar, R.; Carvalho, A.; Amara, K. K.; Zhao, W.; Wang, S.; Toh, M.; Ribeiro, R. M.; Neto, A. H. C.; Matsuda, K.; Eda, G. Photocarrier relaxation pathway in two-dimensional semiconducting transition metal dichalcogenides. *Nature Communications* **2014**, *5*.

(68) Castellanos-Gomez, A.; Vicarelli, L.; Prada, E.; Island, J. O.; Narasimha-Acharya, K.; Blanter, S. I.; Groenendijk, D. J.; Buscema, M.; Steele, G. A.; Alvarez, J., et al. Isolation and characterization of few-layer black phosphorus. *2D Materials* **2014**, *1*, 025001.

(69) Kempt, R. romankempt/hetbuilder: Zenodo Release.

(70) Blum, V.; Gehrke, R.; Hanke, F.; Havu, P.; Havu, V.; Ren, X.; Reuter, K.; Scheffler, M. Ab initio molecular simulations with numeric atom-centered orbitals. *Computer Physics Communications* **2009**, *180*, 2175–2196.

(71) Perdew, J. P.; Burke, K.; Ernzerhof, M. Generalized Gradient Approximation Made Simple. *Physical Review Letters* **1996**, *77*, 3865–3868.

(72) Tkatchenko, A.; Scheffler, M. Accurate Molecular Van Der Waals Interactions from Ground-State Electron Density and Free-Atom Reference Data. *Phys. Rev. Lett.* **2009**, *102*, 073005.